applied sciences

MDPI

Article

Oxygen Vacancy-Mediated ZnO Nanoparticle Photocatalyst for Degradation of Methylene Blue

Qiuping Zhang [1], Ming Xu [1,2,*], Biao You [2], Qin Zhang [1], Huan Yuan [1] and Kostya (Ken) Ostrikov [3,4,*]

1 Key Laboratory of Information Materials of Sichuan Province, School of Electrical and Information Engineering, Southwest University for Nationalities, Chengdu 610041, China; zhqpdq@163.com (Q.Z.); zhq198807@163.com (Q.Z.); yuanhuanwill@126.com (H.Y.)
2 National Laboratory of Solid State Microstructures, Nanjing University, Nanjing 210093, China; youbiao@nju.edu.cn
3 Institute for Future Environments and School of Chemistry, Physics, and Mechanical Engineering, Queensland University of Technology, Brisbane, QLD 4000, Australia
4 CSIRO-QUT Joint Sustainable Processes and Devices Laboratory, P.O. Box 218, Lindfield, NSW 2070, Australia
* Correspondence: hsuming_2001@aliyun.com (M.X.); kostya.ostrikov@qut.edu.au (K.O.)

Received: 4 December 2017; Accepted: 14 January 2018; Published: 28 February 2018

Featured Application: Photocatalyst for degradation of dyes.

Abstract: ZnO nanoparticles (NPs) are synthesized by deoxidizing ZnO powder in a vacuum drying process. This process reduces the size of the NPs and increases the concentration of oxygen vacancies on their surfaces. ZnO NPs with sufficient oxygen vacancies are highly effective for the photodecomposition of methylene blue (MB) dye in water under ultraviolet irradiation. The MB degradation efficiency exceeds 99 percent after 50 min of light irradiation, and the catalytic property of the NPs remains stable over several complete degradation cycles. It is revealed that the concentration of oxygen vacancies on the surface, and the photocatalytic activity, are both higher for smaller NPs. Oxygen vacancies reduce the recombination rate of photo-generated charge carriers by capturing the electrons and hence, improve the efficiency of redox reactions. In addition, a smaller particle size leads to a larger specific surface area and a higher photonic efficiency for the ZnO NPs.

Keywords: semiconductors; surfaces; microstructure; defects

1. Introduction

The relentless escalation in environmental pollution presents a critical and detrimental global problem. In particular, the release of large quantities of toxic dye in wastewater is responsible for the evident and severe destruction of our ecosystem [1]. Semiconductor nanomaterials promise to play a key role in wastewater purification, a prospect that has attracted major attention from the government, industries, and the public. In general, photocatalysis by semiconductors results from the interaction between photo-formed electron and hole pairs on semiconductor surfaces irradiated by UV light [2].

Electrons (e^-) are able to reduce oxygen molecules (O_2) to superoxide (O_2^-), or to hydrogen peroxide (H_2O_2), while some of the holes (h^+) react with H_2O and/or OH^- to produce hydroxyl radicals (•OH). Depending on the actual conditions, the holes, •OH radicals, O_2^-, H_2O_2 and O_2 can all play important roles in photocatalytic reactions [1].

Compared with the traditional wastewater treatment process, semiconductor photocatalysis is a promising way to treat toxic, nocuous, and non-biodegradable contamination in wastewater, at room

temperature and atmospheric pressure [3–5]. While TiO_2 has been investigated extensively [6,7], relatively few photocatalysis studies related to ZnO have been reported.

ZnO, a direct wide-bandgap, semiconducting material, with an energy gap of 3.37 eV, and an exciton binding energy of 60 meV [8], has been harnessed as a multifunctional material to realize numerous technological advances in fields spanning piezoelectronics [9], optics [10], electronics [11], catalysis [12] and photocatalysis [13–17]. Moreover, ZnO may be more efficient than TiO_2 in photocatalytic degradation of some dyes, even in aqueous solutions [18,19].

A lot of recent research has been focused on pure and modified ZnO photocatalytic nanomaterials, including noble metal loading [20], metal and/or nonmetal ion doping [21,22], composite semiconductors [23–25], surface sensitization [26], high-energy ion implantation [27,28], etc. While these methods can widen the spectrum of visible light response and/or lower the recombination rate of electrons/holes, to improve the photocatalytic efficiency, these techniques are not industrially viable as they require costly infrastructure and complex synthesis processes.

Consequently, simpler and more effective treatment methods, such as vacuum deoxidation [29], hydrogen thermal treatment [30,31], and chemical oxidation/reduction [32,33], have been actively pursued for the practical application of ZnO as a photocatalyst. Zhu et al. [29,30] synthesized photocatalysts with a high concentration of oxygen defects by annealing ZnO nanoparticles (NPs) in a He atmosphere at 240~260 °C, or in a H_2 atmosphere at 455~700 °C. These catalytic materials exhibited high activity during the degradation of methylene blue dye, under visible (or UV) light irradiation. By using H_2O_2 aqueous solution to pretreat ZnO powder, Wang et al. [32] obtained ZnO NPs with oxygen vacancies, which was found to be efficient for catalytic decomposition of 2,4-dichlorophenol, under visible light irradiation. However, the safety risk and high cost posed by the utilization of dangerous chemicals (H_2, H_2O_2, etc.) is also bad for mass production of this kind of photocatalyst.

Here, we report on a simple and effective approach to introduce oxygen defects into ZnO materials through a low-temperature, dry vacuum treatment, without any gas. Our ZnO photocatalyst exhibits high photocatalytic activity and good stability during aqueous environmental remediation, and its photocatalytic efficiency is competitive with other reports (Table 1). We further investigated the crystal structure, grain size, and morphology in the as-prepared and treated ZnO samples, and also discuss the relationship between their surface states and photocatalytic properties.

Table 1. Photocatalytic performance of ZnO materials prepared by different processes.

Catalyst	Treatment Condition	Catalyst Concentration (mg/L)	Initial Methylene Blue (MB) Concentration (mg/L)	Irradiation Light Source	Rate Constant (min^{-1})	Ref.
ZnO (commercially available)	H_2 reduction (465 °C/5 h)	500	3.2	11 W UV-light germicidal lamp (λ = 254 nm)	0.1542	[30]
ZnO (commercially available)	He reduction (255 °C/5 h)	500	3.2	11 W UV-light germicidal lamp (λ = 254 nm)	0.1189	[29]
ZnO (commercially available)	Without any gas (250 °C/5 h)	500	5	250 W High-pressure mercury lamp ($\lambda \leq$ 365 nm)	0.1098	This work

2. Experimental

2.1. Synthesis of ZnO Photocatalyst

ZnO powder (analytical grade) was purchased from Tianjin Binhai Cody Chemical Reagent Co., Ltd. Tianjin, China. The preparation of the vacuum-treated ZnO photocatalyst proceeded as follows: 1.5 g of pristine ZnO powder (denoted as Sample A) was loaded into a quartz tube with an opening at one end, and then placed in a vacuum drying oven. It was treated under low vacuum (1 mTorr), provided by a dry pump, for 5 h, at 250 °C (heating rate, 10 °C/min). After the white ZnO powder was vacuum-treated, its color changed to pale yellow. The treated ZnO NPs were denoted as Sample B.

2.2. Characterization

X-ray diffraction (XRD) spectra were recorded on a powder diffractometer (Rigaku DX-2000, Rigaku Co., Tokyo, Japan), with Cu Kα as the X-ray source (λ = 1.5418 Å); the 2-theta range was 20° to 80°, with a step width of 0.01 and count time of 4 s/step. The morphology of samples was characterized by a scanning electron microscope (SEM, JEOL-5900LV, Peabody, MA, USA). The Brunauer–Emmett–Teller (BET) surface area was measured on a Micromeritics ASAP 2020 (Norcross, GA, USA) adsorption apparatus, using N_2 adsorption, at −196 °C. The chemical states of the ZnO samples were characterized by X-ray photoelectron spectroscopy (XPS, PHI 5000 VersaProbe, ULVAC-PHI, Chigasaki, Japan). The electron spin state and the structure of the surface of the ZnO NPs were observed by an electron paramagnetic resonance (EPR) spectrometer (Bruker EMX-10/12, Karlsruhe, Germany), operating in the X-band frequency ($f \approx 9.774$ GHz). Photoluminescence (PL) measurements were conducted in ambient conditions, with a RF-5310pc fluorescence spectrophotometer (Shimadzu, Kyoto, Japan), with an excitation wavelength of 325 nm.

2.3. Photocatalytic Tests

The photocatalytic efficiency of the ZnO samples was evaluated by monitoring the change in optical absorption of a methylene blue (MB) solution, at ~662 nm, during its photocatalytic decomposition process, under UV-light irradiation. Methylene blue ($C_{16}H_{18}N_3SCl$, Color Index No. 52015) exists as a solid, odorless, dark green powder that yields a blue solution when dissolved in water, at room temperature. It is a common contaminant in wastewater released from industrial (e.g., textile) dyeing processes, which is toxic to human health. All the photocatalysis experiments were carried out in a customized photocatalytic reactor, with a 250 W GYZ (HWL-125, Osram Lighting Co., Ltd., Berlin, Germany) as the UV light source ($\lambda \leq 365$ nm), as shown in our previous work [5]. In a typical experiment, 50 mg each of Sample A and Sample B were dispersed, respectively, into 100 mL of MB aqueous solution (4 mg/L), in 250 mL glass beakers. Before exposing the solutions to UV-light, they were ultrasonicated for 30 s, magnetically stirred for 20 min, and then kept in darkness for 0.5 h, to establish an adsorption–desorption equilibrium.

The system was then exposed to UV-light. At 10 min intervals, 5 mL aliquots were taken out and centrifuged (5000 rpm, 5 min) to remove the catalyst from the suspension. The absorbance of MB was monitored by a UV-vis spectrophotometer. We used the following equation to calculate the degradation rate:

$$X = (A_0 - A_t)/A_0 \times 100\% \quad (1)$$

where A_0 is the absorbance of dyes before illumination and A_t is the absorbance of dyes at time, t.

For multi-cycle performance tests, once the photocatalytic reaction of a testing cycle is complete, the subsequent cycle is then started, after an aliquot of 5 mL of MB mother liquor (80 mg/L) and deionized water are added to the glass beaker, to bring the concentration of the solution to approximately 4 mg/L. The length of each cycle was 100 min.

3. Results and Discussion

3.1. XRD and SEM Analysis

The XRD spectra of different ZnO NPs is shown in Figure 1. Three major peaks, observed at $2\theta \approx 31.8°$, 34.5°, and 36.3°, can be assigned to the (100), (002) and (101) lattice planes, respectively, which is in a good agreement with the standard JCPDS file No. 36-1451 for ZnO [34]. This reveals that Sample A and Sample B both belong to the hexagonal wurtzite structure with the space group P63mc [35]. No change occurred in the structure of ZnO during the vacuum treatment. The average grain sizes of the two samples, according to the Scherrer's equation, were both about 60 nm.

As shown in SEM images (Figure 2), ZnO samples are composed of particles with a hexagonal rod shape and relatively uniform particle size distribution. The crystal structure and morphology of

the ZnO NPs are generally unchanged after the vacuum treatment. This is consistent with the results obtained by XRD (Figure 1). However, the average particle size (~150 nm) of Sample B is slightly smaller than those (~200 nm) of Sample A, owning to a decrease in particle aggregation—the smaller the particle size, the larger the specific surface area. The BET measurement shows that the specific surface areas of Sample A and Sample B are 4.29 and 6.34 m^2/g, respectively.

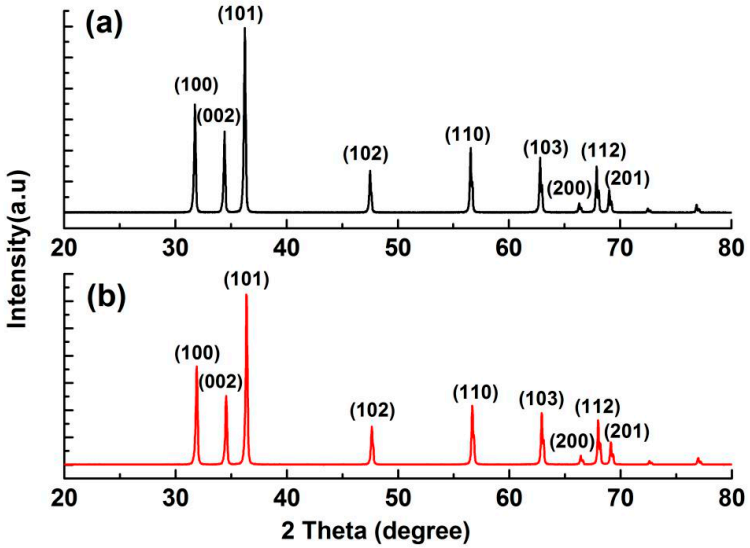

Figure 1. XRD spectra of different ZnO nanoparticles (NPs): (**a**) Sample A; (**b**) Sample B.

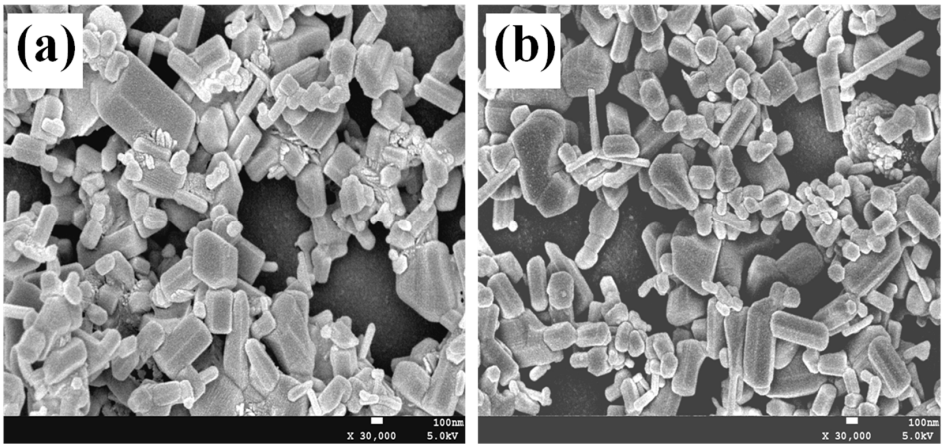

Figure 2. SEM micrographs of different ZnO NPs: (**a**) Sample A; (**b**) Sample B.

3.2. XPS Analysis

To determine the chemical state of the ZnO nanoparticle surfaces, XPS measurements were performed. From Figure 3, one can find that the energy differences between the Zn $2p_{3/2}$ and Zn $2p_{1/2}$ peaks of the two samples are 23.09 and 23.11 eV, respectively. These values are within the range of the XPS standard reference value of ZnO [36]. The Zn 2p XPS peak is sharp, and its corresponding binding energy indicates the presence of Zn^{2+} lattice ions [37].

Figure 4 shows that O 1s core level spectra are quite asymmetric, with a broad shoulder by the side of the higher binding energy, indicative of oxygen-rich states (–OH, H_2O, O_2, etc.) on the surface [38]. The O 1s spectra of ZnO NPs can be described as the superposition of two Gaussian peaks. The main peak, at about 530.1 ± 0.1 eV, is attributed to oxygen in the ZnO crystal lattice (O_L) [39,40], while the

second peak, at a higher binding energy (O_H) of 532.0 ± 0.1 eV, is related to the presence of hydroxyl groups (–OH) [37].

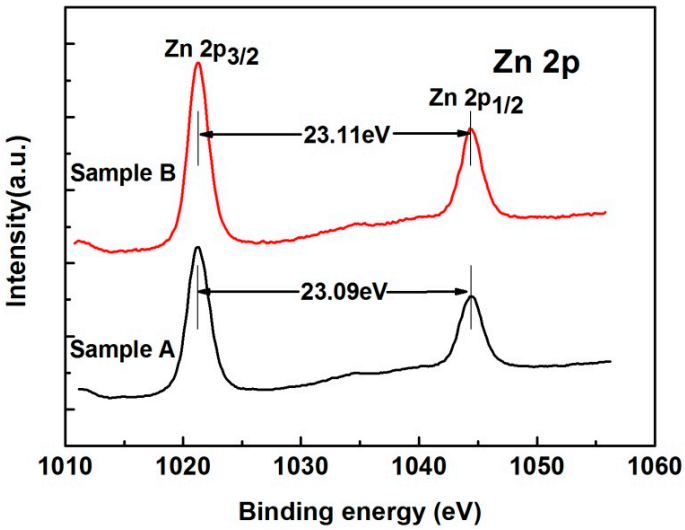

Figure 3. Zn 2p XPS spectra of different ZnO NPs.

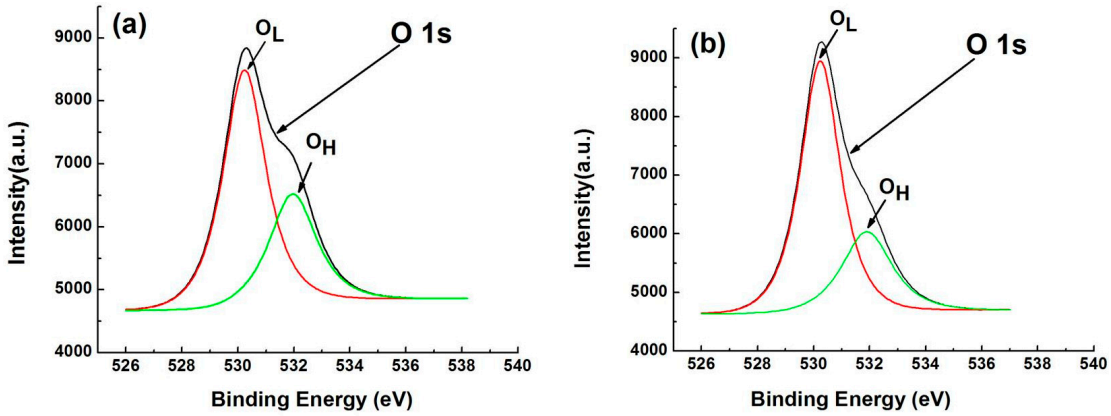

Figure 4. O 1s XPS spectra of different ZnO NPs: (**a**) Sample A; (**b**) Sample B.

The XPS data of Zn 2p and O 1s of the vacuum-treated and pristine ZnO NPs are shown in Table 2. As the atomic ratio of Zn to O_L at the surface of the samples is much higher than 1.0, this suggests that there are many oxygen vacancies at the surface of the ZnO NPs. An oxygen vacancy acts as an active site, which can easily combine and form stable structures with other active species [37]. This accounts for the high fraction of hydroxyl groups adsorbed on the ZnO surface. In addition, the atomic ratios of Zn to O_L and O_L to O_H on the surface of Sample B are both higher than those of Sample A. Therefore, the concentration of oxygen vacancies in ZnO increases when pristine ZnO is treated. One possible reason for this is that a large number of hydroxyl groups are desorbed from the ZnO surface and then pumped out of the vacuum chamber.

Table 2. XPS data of oxygen and zinc elements at the surface of different ZnO NPs.

ZnO Sample	Binding Energy of Oxygen (eV)		The Atomic Ratio of O_L to O_H	The Atomic Ratio of Zn to O_L
	O_L	O_H		
Sample A	530.288	531.955	2.02	1.39
Sample B	530.240	531.903	2.56	1.51

3.3. EPR Analysis

To further confirm the XPS results, EPR measurements were performed for two samples. Figure 5 shows the EPR spectra of different ZnO NPs, recorded at room temperature. One can see that the—EPR signal (g = 1.9568) intensity is the same in both samples.

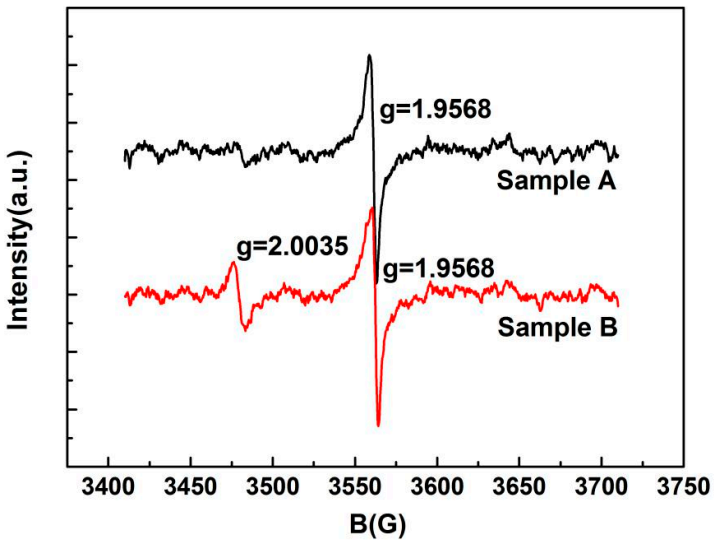

Figure 5. EPR spectrum of different ZnO NPs at room temperature (f = 9.774 GHz).

However, a significant EPR signal with a g factor of 2.0035 was detected in Sample B. This is commonly attributed to an unpaired electron trapped in an oxygen vacancy site [41–43]. Hence, a stronger g-2.0035 EPR signal corresponds to the higher concentration of oxygen vacancies in ZnO. The surface of Sample B has more oxygen vacancies than the surface of Sample A.

3.4. PL Analysis

Figure 6 shows the room temperature PL spectrum of different ZnO NPs, where the pristine and vacuum-treated ZnO both display strong UV and weak visible emission peaks, at 384 and 470 nm, respectively. The UV emission is attributed to the direct recombination of free excitons [5]. The blue–green (470 nm) emission implies that electrons trapped by the oxygen vacancies recombine with photo-generated holes [5,29]. This further confirms the existence of oxygen defects on the surface of the ZnO photocatalyst. Compared with Sample A, Sample B, with a higher concentration of surface oxygen vacancies, shows stronger visible, and lower UV, PL signals, which indicates an increase in the separation rate of photo-generated electron-hole pairs by oxygen vacancies.

3.5. Photocatalytic Efficiency

3.5.1. Comparison of Catalytic Activity

In general, dye molecules are gradually adsorbed on the surface of a catalyst, before the photocatalytic reactions occur, and ultimately reach saturation. According to Equation (1), the percentages of MB absorbed on the surfaces of Sample A and Sample B during its adsorption–desorption process (30 min), were 2.3% and 4.2%, respectively. This clearly shows that a large number of oxygen vacancies on the surface of ZnO NPs contribute to the adsorption of dye molecules onto the photocatalytic surface. Figure 7a shows the decomposition of MB (4 mg/L), using different ZnO nano-catalysts exposed to UV light. Remarkably, MB is unstable under UV irradiation, and over 13% of the dye was photo-decomposed, even in the absence of a catalyst.

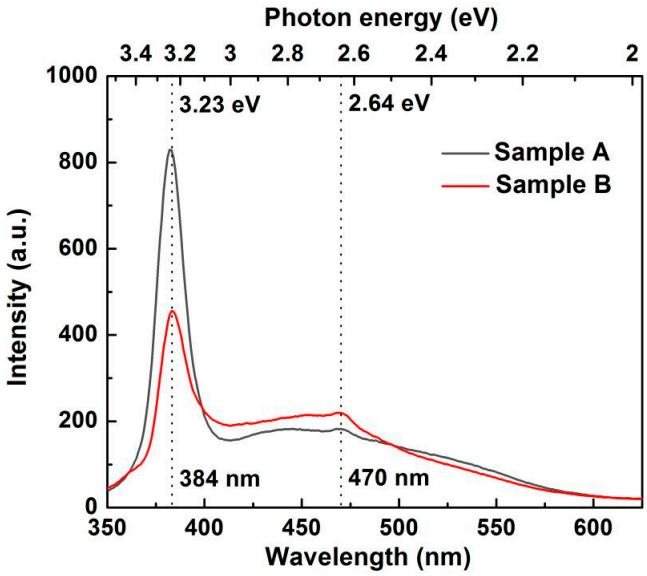

Figure 6. Room temperature photoluminescence (PL) spectrum of different ZnO NPs, at 325 nm excitation.

Therefore, the decomposition of MB is related to photolysis of itself and photocatalytic oxidation of the ZnO catalyst, in which absorption of the dye molecules and photocatalysis both occur on the surface of the catalyst. Without considering adsorption, photodegradation was complete (over 99% of MB was degraded) after 50 min for Sample B, whereas Sample A, under the same testing conditions, took nearly 80 min. Photodegradation of various dyes fits a pseudo first-order kinetic model [44]:

$$\mathrm{Ln}\,(C_0/C_t) = k_{app}\,t \tag{2}$$

where C_0 is the concentration of dyes before illumination and C_t is the concentration of dyes at time, t, and k_{app} is the apparent rate constant.

Figure 7b shows that the photodegradation of MB, in both Sample A and Sample B, conforms to the pseudo first-order kinetics approximation. The rate constants are calculated to be 0.091 ± 0.005 min^{-1} (R = 0.989) and 0.110 ± 0.005 min^{-1} (R = 0.996), respectively. The above results indicate that photocatalytic efficiency in photodecomposing MB is higher for vacuum-treated ZnO NPs than for pristine ZnO NPs. The improvement in photocatalytic efficiency is due to the decrease in particle size, caused by the reduction in particle aggregation and the increase in surface oxygen vacancies.

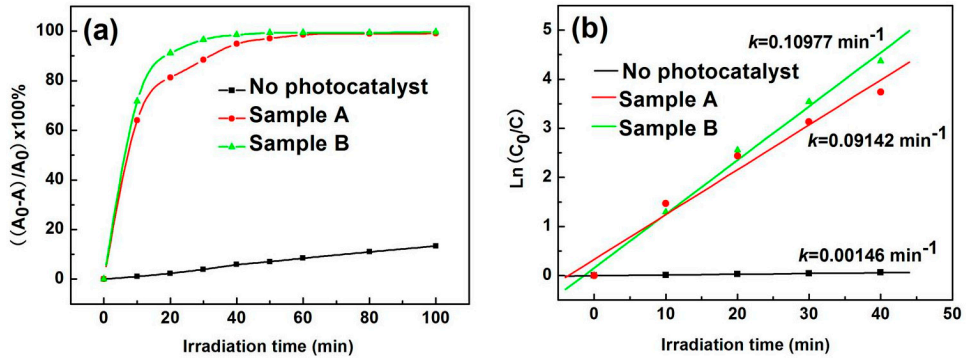

Figure 7. (**a**) Extent of decomposition of MB, over time, in the presence of different ZnO NPs and (**b**) the pseudo first-order kinetics curve.

3.5.2. Catalytic Stability of Vacuum-Treated ZnO NPs

Both the stability and recyclability of photocatalysts are extremely important for practical applications. Figure 8 shows the results of cycling tests of the UV-light driven photocatalytic activity of Sample B in degrading MB. Sample B shows good photocatalytic activity under UV-light irradiation, and no appreciable loss of activity after eight cycles. The remarkable photocatalytic stability of the vacuum-treated ZnO NPs indicates its feasibility in practical applications.

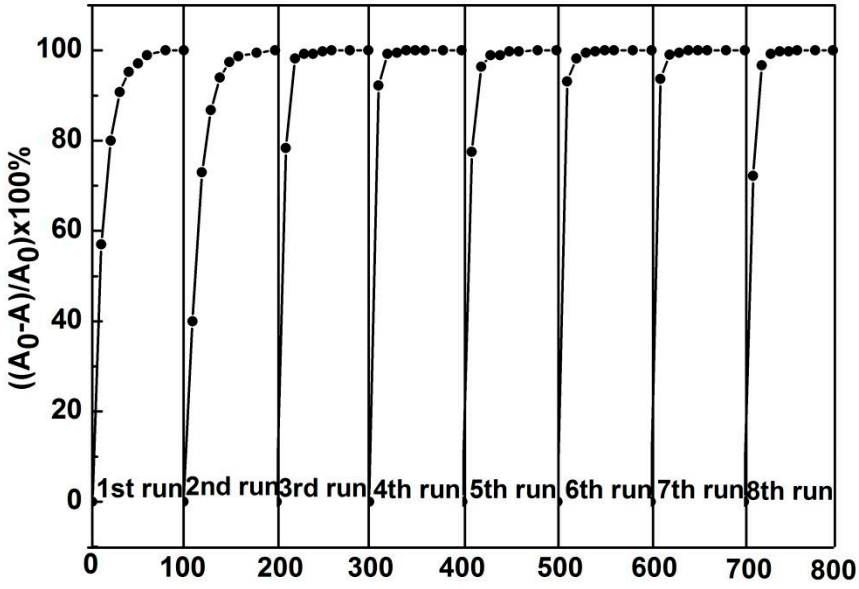

Figure 8. Cycling tests for photocatalytic degradation of MB, using Sample B, under UV-light irradiation.

3.6. Photocatalytic Mechanism

The mechanism for the photocatalytic degradation of MB with a ZnO photocatalyst is shown in Figure 9. The effectiveness of ZnO NPs in MB decomposition can be explained on the basis of the •OH radicals and holes present on the surface of ZnO NPs, which break down MB dye in aqueous solutions.

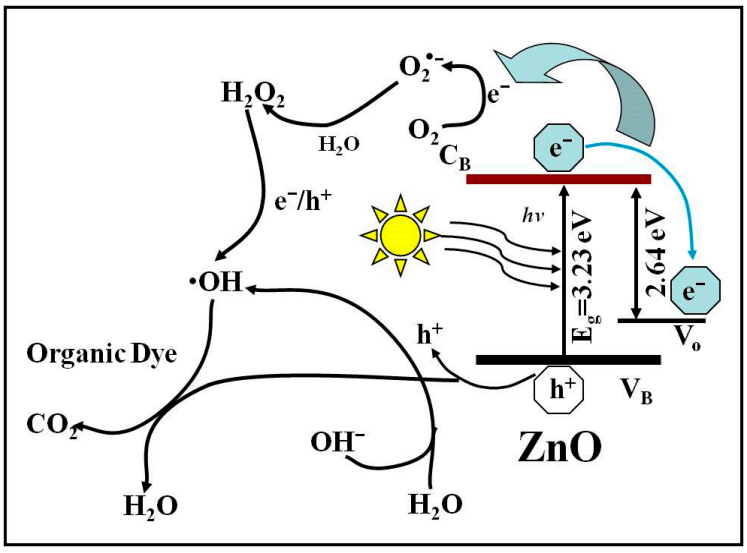

Figure 9. Schematic of ZnO NP photocatalytic processes.

When a semiconductor particle absorbs a photon with an energy ($h\nu$) matching or exceeding its bandgap energy (E_g), an electron (e_{cb}^-) is excited from the valence band (V_B) to the conduction band (C_B), leaving a hole (h_{vb}^+) behind. The photo-generated electrons and holes can recombine and dissipate the input energy as heat, get trapped in metastable surface states, or react with electron donors and acceptors adsorbed on the semiconductor surface or within the surrounding double electrical layer of charged particles [14]. However, surface defect states, related to oxygen vacancies, are available to trap electrons or holes. Thus, the probability of recombination is reduced and subsequent redox reactions may occur.

As mentioned above, oxygen vacancies play an important role in the degradation of dye under UV-light irradiation. They create an impurity level between the C_B and V_B of the vacuum-treated ZnO, which acts as a deep donor defect level, near the top of V_B [45]. The V_o defect energy levels used in Figure 9 are obtained by calculating the emission energy (2.64 eV) corresponding to the peak around 470 nm (PL spectrum shown in Figure 6). The calculated bandgap energy of 3.23 eV corresponds to the band-edge emission peak at around 384 nm, as shown in Figure 6. Indeed, an "empty" oxygen site (V_o^{2+}) can trap either one (V_o^+) or two (V_o^0) electrons [41], thereby effectively reducing the recombination rate of the e_{cb}^-–h_{vb}^+ pairs. More e_{cb}^- and h_{vb}^+ migrate to the surface of the vacuum-treated ZnO and promote the photocatalytic degradation reactions.

Moreover, particle size and photocatalytic activity are related. In particular, semiconductor NPs exhibit quantum size effects as the particle size decreases. This size reduction may improve the photocatalytic efficiency by increasing the effective bandgap [46]. In addition, reducing the particle size leads to a larger specific surface area. The latter is defined as the total surface area used in the redox reaction, with a corresponding increase in the number of active sites exposed. A decrease in particle size should also lead to higher photonic efficiency, due to a higher interfacial charge carrier transfer rate [47].

For wastewater treatment, dispersibility of the catalyst is another performance factor. As more catalyst particles are dispersed in the liquid, the total reaction surface area increases and this leads to a higher light harvesting efficiency. This will promote the adsorption of molecules on the surface of the catalytic particles. Consequently, the overall photocatalytic efficiency of the pristine ZnO NPs increases after vacuum treatment.

4. Conclusions

In summary, pale yellow ZnO nanoparticles (NPs) have been synthesized, using a vacuum drying process, to deoxidize ZnO powder. In comparison with pristine ZnO NPs, this vacuum treatment technique results in smaller ZnO NP sizes and an increase in oxygen vacancies. Moreover, these vacuum-treated ZnO NPs preserve their pristine crystal structures. In photocatalytic experiments under UV-light irradiation, the vacuum-treated ZnO NPs exhibit better photocatalytic activity (over 99% of MB is degraded after 50 min UV irradiation time, with the effective reaction rate $k_{app} \approx 0.10977\ \text{min}^{-1}$) and stability (excellent photocatalytic activity still exists after eight cycles) in the process of photodecomposing MB. The SEM, BET XPS, EPR and PL characterizations suggest that the observed higher photocatalytic activity of the vacuum-treated ZnO NPs stems from the smaller particle sizes and the abundance of oxygen vacancies on their surfaces.

Acknowledgments: This work is supported by Foundation of Science and Technology Bureau of Sichuan Province (Grant No. 2017JY0349) and National Laboratory of Solid State Microstructures, Nanjing University (Grant No. M30016), China. Kostya (Ken) Ostrikov was partially supported by the Australian Research Council and CSIRO's Science Leadership Program.

Author Contributions: Qiuping Zhang and Ming Xu conceived and designed the experiments; Qiuping Zhang performed the experiments; Qiuping Zhang, Ming Xu and Kostya (Ken) Ostrikov analyzed the data; Biao You contributed reagents/materials/analysis tools; Qin Zhang and Huan Yuan took part in the experiment work; all authors took part in the manuscript preparation.

Conflicts of Interest: The authors declare no conflict of interest.

References

1. Kaneko, M.; Okura, I. *Photocatalysis Science and Technology*; Springer: Berlin/Heidelberg, Germany, 2002.
2. Ji, P.; Takeuchi, M.; Cuong, T.M.; Zhang, J.; Matsuoka, M.; Anpo, M. Recent advances in visible light-responsive titanium oxide-based photocatalysts. *Res. Chem. Intermed.* **2010**, *36*, 327–347. [CrossRef]
3. Hoffmann, M.R.; Martin, S.T.; Choi, W.; Bahnemann, D.W. Environmental Applications of Semiconductor Photocatalysis. *Chem. Rev.* **1995**, *95*, 69–96. [CrossRef]
4. Fujishima, A.; Zhang, X.; Tryk, D.A. TiO_2 photocatalysis and related surface phenomena. *Surf. Sci. Rep.* **2008**, *63*, 515–582. [CrossRef]
5. Zhang, Q.P.; Xu, X.N.; Liu, Y.T.; Xu, M.; Deng, S.H.; Chen, Y.; Yuan, H.; Yu, F.; Huang, Y.; Zhao, K.; et al. A feasible strategy to balance the crystallinity and specific surface area of metal oxide nanocrystals. *Sci. Rep.* **2017**, *7*. [CrossRef] [PubMed]
6. Guo, Z.; Ma, R.; Li, G. Degradation of phenol by nanomaterial TiO_2 in wastewater. *Chem. Eng. J.* **2006**, *119*, 55–59. [CrossRef]
7. Zhao, D.; Wang, D.; Shi, H.; Yan, X. Study on photocatalytic oxidation of p-chlorophenol with transition metal-doped TiO_2 nanoparticles. *Environ. Prot. Chem. Ind.* **2003**, *23*, 4–7.
8. Moezzi, A.; McDonagh, A.M.; Cortie, M.B. Zinc oxide particles: Synthesis, properties and applications. *Chem. Eng. J.* **2012**, *185*, 1–22. [CrossRef]
9. Wang, Z.L.; Song, J. Piezoelectric nanogenerators based on zinc oxide nanowire arrays. *Science* **2006**, *312*, 242–246. [CrossRef] [PubMed]
10. Huang, M.H.; Mao, S.; Feick, H.; Yan, H.; Wu, Y.; Kind, H.; Weber, E.; Russo, R.; Yang, P. Room-Temperature Ultraviolet Nanowire Nanolasers. *Science* **2001**, *292*, 1897–1899. [CrossRef] [PubMed]
11. Tsukazaki, A.; Ohtomo, A.; Onuma, T.; Ohtani, M.; Makino, T.; Sumiya, M.; Ohtani, K.; Chichibu, S.F.; Fuke, S.; Segawa, Y.; et al. Repeated temperature modulation epitaxy for p-type doping and light-emitting diode based on ZnO. *Nat. Mater.* **2004**, *4*, 42–46. [CrossRef]
12. Shido, T.; Iwasawa, Y. Reactant-promoted reaction mechanism for water-gas shift reaction on ZnO, as the genesis of surface catalysis. *J. Catal.* **1991**, *129*, 343–355. [CrossRef]
13. Kuo, T.J.; Lin, C.N.; Kuo, C.L.; Huang, M.H. Growth of Ultralong ZnO Nanowires on Silicon Substrates by Vapor Transport and Their Use as Recyclable Photocatalysts. *Chem. Mater.* **2007**, *19*, 5143–5147. [CrossRef]
14. Wang, J.; Liu, P.; Fu, X.; Li, Z.; Han, W.; Wang, X. Relationship between Oxygen Defects and the Photocatalytic Property of ZnO Nanocrystals in Nafion Membranes. *Langmuir* **2008**, *25*, 1218–1223. [CrossRef] [PubMed]
15. Li, Y.; Xie, W.; Hu, X.; Shen, G.; Zhou, X.; Xiang, Y.; Zhao, X.; Fang, P. Comparison of Dye Photodegradation and its Coupling with Light-to-Electricity Conversion over TiO_2 and ZnO. *Langmuir* **2009**, *26*, 591–597. [CrossRef] [PubMed]
16. Akyol, A.; Yatmaz, H.C.; Bayramoglu, M. Photocatalytic decolorization of Remazol Red RR in aqueous ZnO suspensions. *Appl. Catal. B* **2004**, *54*, 19–24. [CrossRef]
17. Xu, X.N.; Zhang, Q.P.; Ong, B.T.M.; Yuan, H.; Chen, Y.; Liu, Y.T.; Xu, M. Influence of stabilizer on the microstructures and photocatalytic performance of ZnO nanopowder synthesized by Sol-gel method. *J. Nano Res.* **2017**, *50*, 57–71. [CrossRef]
18. Gouvêa, C.A.K.; Wypych, F.; Moraes, S.G.; Durán, N.; Nagata, N.; Perlta-Zamora, P. Semiconductor-assisted photocatalytic degradation of reactive dyes in aqueous solution. *Chemosphere* **2000**, *40*, 433–440. [CrossRef]
19. Dindar, B.; Icli, S. Unusual photoreactivity of zinc oxide irradiated by concentrated sunlight. *J. Photochem. Photobiol. A* **2001**, *140*, 263–268. [CrossRef]
20. Han, Z.; Ren, L.; Cui, Z.; Chen, C.; Pan, H.; Chen, J. Ag/ZnO flower heterostructures as a visible-light driven photocatalyst via surface Plasmon resonance. *Appl. Catal. B* **2012**, *126*, 298–305. [CrossRef]
21. Li, D.; Haneda, H.; Ohashi, N.; Saito, N.; Hishita, S. Morphological reform of ZnO particles induced by coupling with MO_x (M=V, W, Ce) and the effects on photocatalytic activity. *Thin Solid Films* **2005**, *486*, 20–23. [CrossRef]
22. Shinde, S.S.; Bhosale, C.H.; Rajpure, K.Y. Photocatalytic degradation of toluene using sprayed N-doped ZnO thin films in aqueous suspension. *J. Photochem. Photobiol. B* **2012**, *113*, 70–77. [CrossRef] [PubMed]

23. Uddin, M.T.; Nicolas, Y.; Olivier, C.; Toupance, T.; Servant, L.; Müller, M.M.; Kleebe, H.J.; Ziegler, J.; Jaegermann, W. Nanostructured SnO_2-ZnO Heterojunction Photocatalysts Showing Enhanced Photocatalytic Activity for the Degradation of Organic Dyes. *Inorg. Chem.* **2012**, *51*, 7764–7773. [CrossRef] [PubMed]
24. Cheng, C.; Amini, A.; Zhu, C.; Xu, Z.; Song, H.; Wang, N. Enhanced photocatalytic performance of TiO_2-ZnO hybrid nanostructures. *Sci. Rep.* **2014**, *4*, 4181. [CrossRef] [PubMed]
25. Kant, S.; Pathania, D.; Singh, P.; Dhiman, P.; Kumar, A. Removal of malachite green and methylene blue by $Fe_{0.01}Ni_{0.01}Zn_{0.98}O$/polyacrylamide nanocomposite using coupled adsorption and photocatalysis. *Appl. Catal. B* **2014**, *147*, 340–352. [CrossRef]
26. Yang, G.C.C.; Chan, S.W. Photocatalytic reduction of chromium(VI) in aqueous solution using dye-sensitized nanoscale ZnO under visible light irradiation. *J. Nanopart. Res.* **2009**, *11*, 221–230. [CrossRef]
27. Wang, M.; Ren, F.; Cai, G.; Liu, Y.; Shen, S.; Guo, L. Activating ZnO nanorod photoanodes in visible light by Cu ion implantation. *Nano Res.* **2014**, *7*, 353–364. [CrossRef]
28. Cai, L.; Ren, F.; Wang, M.; Cai, G.; Chen, Y.; Liu, Y.; Shen, S.; Guo, L. V ions implanted ZnO nanorod arrays for photoelectrochemical water splitting under visible light. *Int. J. Hydrog. Energy* **2015**, *40*, 1394–1401. [CrossRef]
29. Lv, Y.; Pan, C.; Ma, X.; Zong, R.; Bai, X.; Zhu, Y. Production of visible activity and UV performance enhancement of ZnO photocatalyst via vacuum deoxidation. *Appl. Catal. B* **2013**, *138*, 26–32. [CrossRef]
30. Lv, Y.; Yao, W.; Ma, X.; Pan, C.; Zong, R.; Zhu, Y. The surface oxygen vacancy induced visible activity and enhanced UV activity of a ZnO_{1-x} photocatalyst. *Catal. Sci. Technol.* **2013**, *3*, 3136–3146. [CrossRef]
31. Xia, T.; Wallenmeyer, P.; Anderson, A.; Murowchick, J.; Liu, L.; Chen, X. Hydrogenated black ZnO nanoparticles with enhanced photocatalytic performance. *RSC Adv.* **2014**, *4*, 41654–41658. [CrossRef]
32. Wang, J.; Wang, Z.; Huang, B.; Ma, Y.; Liu, Y.; Qin, X.; Zhang, X.; Dai, Y. Oxygen vacancy induced band-gap narrowing and enhanced visible light photocatalytic activity of ZnO. *ACS Appl. Mater. Interfaces* **2012**, *4*, 4024–4030. [CrossRef] [PubMed]
33. Guo, H.L.; Zhu, Q.; Wu, X.L.; Jiang, Y.F.; Xie, X.; Xu, A.W. Oxygen deficient ZnO_{1-x} nanosheets with high visible light photocatalytic activity. *Nanoscale* **2015**, *7*, 7216–7223. [CrossRef] [PubMed]
34. Zhang, W.H.; Zhang, W.D. Fabrication of SnO_2-ZnO nanocomposite sensor for selective sensing of trimethylamine and the freshness of fishes. *Sens. Actuators B* **2008**, *134*, 403–408. [CrossRef]
35. Sahal, M.; Hariti, B.; Ridah, A.; Mollar, M.; Mari, B. Structural, electrical and optical properties of ZnO thin films deposited by sol-gel method. *Microelectron. J.* **2008**, *39*, 1425–1428. [CrossRef]
36. Wanger, C.D.; Riggs, W.M.; Davis, L.E.; Moulder, J.F. *Handbook of X-Ray Photoelectron Spectroscopy*; Perkin Elmer: Waltham, MA, USA, 1979; p. 2919.
37. Jing, L.; Xu, Z.; Sun, X.; Shang, J.; Cai, W. The surface properties and photocatalytic activities of ZnO ultrafine particles. *Appl. Surf. Sci.* **2001**, *180*, 308–314. [CrossRef]
38. Pei, Z.; Ding, L.; Hu, J.; Weng, S.; Zheng, Z.; Huang, M.; Liu, P. Defect and its dominance in ZnO films: A new insight into the role of defect over photocatalytic activity. *Appl. Catal. B* **2013**, *142*, 736–743. [CrossRef]
39. Chen, M.; Wang, X.; Yu, Y.H.; Pei, Z.L.; Bai, X.D.; Sun, C.; Huang, R.F.; Wen, L.S. X-ray photoelectron spectroscopy and auger electron spectroscopy studies of Al-doped ZnO films. *Appl. Surf. Sci.* **2000**, *158*, 134–140. [CrossRef]
40. Hsieh, P.T.; Chen, Y.C.; Kao, K.S.; Wang, C.M. Luminescence mechanism of ZnO thin film investigated by XPS measurement. *Appl. Phys. A Mater. Sci. Process.* **2008**, *90*, 317–321. [CrossRef]
41. Ischenko, V.; Polarz, S.; Grote, D.; Stavarache, V.; Fink, K.; Driess, M. Zinc Oxide Nanoparticles with Defects. *Adv. Funct. Mater.* **2005**, *15*, 1945–1954. [CrossRef]
42. Zhuang, J.; Weng, S.; Dai, W.; Liu, P.; Liu, Q. Effects of Interface Defects on Charge Transfer and Photoinduced Properties of TiO_2 Bliayer Films. *J. Phys. Chem. C* **2012**, *116*, 25354–25361. [CrossRef]
43. Liu, H.; Ma, H.T.; Li, X.Z.; Li, W.Z.; Wu, M.; Bao, X.H. The enhancement of TiO_2 photocatalytic activity by hydrogen thermal treatment. *Chemosphere* **2003**, *50*, 39–46. [CrossRef]
44. Bai, H.; Liu, Z.; Sun, D.D. Hierarchical ZnO/Cu "corn-like" materials with high photodegradation and antibacterial capability under visible light. *Phys. Chem. Chem. Phys.* **2011**, *13*, 6205–6210. [CrossRef] [PubMed]
45. Zhang, C.; Geng, X.; Liao, H.; Li, C.J.; Debliquy, M. Room-temperature nitrogen-dioxide sensors based on ZnO_{1-x} coatings deposited by solution precursor plasma spray. *Sens. Actuators B* **2017**, *242*, 102–111. [CrossRef]

46. Li, Y.; Lu, G.; Li, S. Research advances of photocatalytic decomposition of water by semiconductor. *J. Mol. Catal. (China)* **2001**, *15*, 72–79.
47. Zhang, Z.; Wang, C.C.; Zakaria, R.; Yang, J.Y. Role of Particle Size in Nanocrystalline TiO_2-Based Photocatalysts. *J. Phys. Chem. B* **1998**, *102*, 10871–10878. [CrossRef]